This is a repository copy of *Solid-State 19F NMR Chemical Shift in Square-Planar Nickel-Fluoride Complexes Linked by Halogen Bonds*.

White Rose Research Online URL for this paper:
https://eprints.whiterose.ac.uk/202041/

Version: Published Version

Article

Solid-State ^{19}F NMR Chemical Shift in Square-Planar Nickel–Fluoride Complexes Linked by Halogen Bonds

Abril C. Castro,* Michele Cascella, Robin N. Perutz, Christophe Raynaud,* and Odile Eisenstein*

Read Online

ACCESS | Metrics & More | Article Recommendations | Supporting Information

ABSTRACT: The halogen bond (XB) is a highly directional class of noncovalent interactions widely explored by experimental and computational studies. However, the NMR signature of the XB has attracted limited attention. The prediction and analysis of the solid-state NMR (SSNMR) chemical shift tensor provide useful strategies to better understand XB interactions. In this work, we employ a computational protocol for modeling and analyzing the ^{19}F SSNMR chemical shifts previously measured in a family of square-planar *trans* Ni^{II}-L$_2$-iodoaryl-fluoride (L = PEt$_3$) complexes capable of forming self-complementary networks held by a NiF···I(C) halogen bond [Thangavadivale, V.; et al. *Chem. Sci.* **2018**, *9*, 3767−3781]. To understand how the ^{19}F NMR resonances of the nickel-bonded fluoride are affected by the XB, we investigate the origin of the shielding in *trans*-[NiF(2,3,5,6-C$_6$F$_4$I)(PEt$_3$)$_2$], *trans*-[NiF(2,3,4,5-C$_6$F$_4$I)(PEt$_3$)$_2$], and *trans*-[NiF(C$_6$F$_5$)(PEt$_3$)$_2$] in the solid state, where a XB is present in the two former systems but not in the last. We perform the ^{19}F NMR chemical shift calculations both in periodic and molecular models. The results show that the crystal packing has little influence on the NMR signatures of the XB, and the NMR can be modeled successfully with a pair of molecules interacting via the XB. Thus, the observed difference in chemical shift between solid-state and solution NMR can be essentially attributed to the XB interaction. The very high shielding of the fluoride and its driving contributor, the most shielded component of the chemical shift tensor, are well reproduced at the 2c-ZORA level. Analysis of the factors controlling the shielding shows how the highest occupied Ni/F orbitals shield the fluoride in the directions perpendicular to the Ni−F bond and specifically perpendicular to the coordination plane. This shielding arises from the magnetic coupling of the Ni(3d)/F(2p lone pair) orbitals with the vacant σ^*_{Ni-F} orbital, thereby rationalizing the very highly upfield (shielded) resonance of the component (δ_{33}) along this direction. We show that these features are characteristic of square-planar nickel−fluoride complexes. The deshielding of the fluoride in the halogen-bonded systems is attributed to an increase in the energy gap between the occupied and vacant orbitals that are mostly responsible for the paramagnetic terms, notably along the most shielded direction.
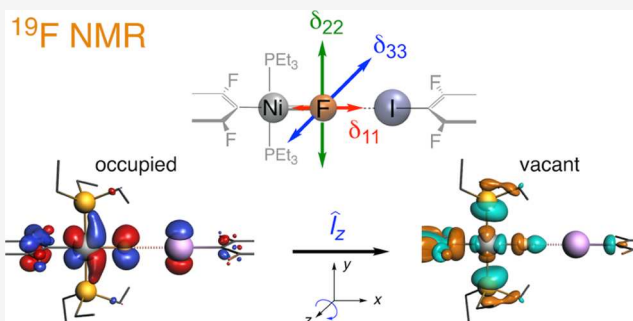
INTRODUCTION

The halogen bond (XB) is a stabilizing noncovalent interaction involving halogen atoms. It is constituted by an electrophilic region, associated with a covalently bonded halogen atom called the XB donor, and a nucleophilic region, typically a Lewis base, called the XB acceptor.[1] Similar in energy to the more prominent hydrogen bonds,[2,3] XBs form highly directional interactions, exploited by many applications in supramolecular chemistry, crystal engineering, materials design, and biological systems.[4−6] The nature of the XB, which has attracted considerable interest from the theoretical community, has been debated for many years.[7−17] Clark, et al. introduced the concept of the σ-hole, that is, the emergence of a region of positive electrostatic potential along the extension of the covalently bonded halogen atom, to account for the electrophilic behavior of a halogen in an attractive interaction toward diverse Lewis bases.[18] However, this concept could not describe XBs in full. Numerous theoretical studies have

shown that charge transfer, electrostatics, dispersion, and polarization interactions contribute to the XB.[8,9,14−17,19−21]

While the XB has been probed by diverse spectroscopic techniques,[22−26] nuclear magnetic resonance (NMR) spectroscopy has been especially useful as it can detect the interaction either in solution[6] or in the solid state,[5] both for organic molecules[27,28] and for transition-metal-containing systems.[29] Due to the high XB donor strength of iodine, the majority of the studies have been carried out with an organic species bearing a C−I bond, while a wide variety of Lewis bases have been used as XB acceptor. Overall, the ^{13}C NMR
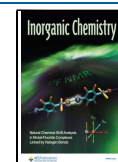
resonance of the C−I bond is deshielded by the XB, while the chemical shifts of the XB acceptors depend on their molecular nature. However, using the C−I bond length as criterion, a correlation between chemical shifts and XB strength was established.[5] In contrast, no clear relationship appeared between NMR chemical shifts and distances between the XB donor and acceptor, even though the chemical shifts of the atoms involved in the XB are known to be sensitive to structural features.[30−32] So far, few studies concerned the relationship between the NMR chemical shift at atoms involved in the XB and variations in molecular properties of the XB donor and acceptor.[33]

The fact that metal−fluoride complexes can form strong hydrogen bonds and XBs demonstrated that the fluoride can act as a potent Lewis base and that the thermodynamics of the XB was measurable and highly sensitive to the chemical nature of the metal−ligand complex.[34−38] Investigations of XB interactions involving metal centers are thus particularly useful because their strength can be tuned by changing either the inorganic halogen (M−X) acting as XB acceptor or the organic halogen (C−X′) acting as XB donor.[29] Furthermore, the metal−fluoride complexes are of special interest because they exhibit a ^{19}F NMR resonance that lies upfield away from all of the other ^{19}F resonances and is acutely responsive to the chemical environment. Importantly, the fluorine resonance is deshielded in the presence of a XB by up to 25−40 ppm and can thus be an ideal reporter for the XB characteristics. In particular, the solid-state NMR (SSNMR) study of Ni^{II}−fluoride complexes that form self-complementary networks[39] offers information on the anisotropy of the fluorine chemical shift; comparable ^{19}F SSNMR measurements are rather rare.[40,41] The effect of the XB on the ^{19}F SSNMR chemical shift was demonstrated by comparing the NMR spectra of trans-[NiF(2,3,5,6-C$_6$F$_4$I)(PEt$_3$)$_2$] 1pF and trans-[NiF(2,3,4,5-C$_6$F$_4$I)(PEt$_3$)$_2$] 1oF complexes, with that of a complex incapable of XB formation, trans-[NiF(C$_6$F$_5$)(PEt$_3$)$_2$] 3F[42] (Figure 1). For 1pF and 1oF, the presence of the XB is
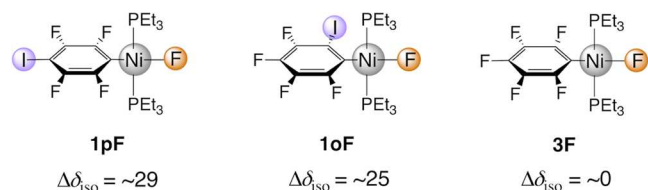
Figure 1. Nickel−fluoride complexes considered in this work.[39,42] The experimental $\Delta\delta_{iso}$ values (in ppm) give the difference between the solid-state and solution ^{19}F NMR resonances of the nickel-bonded fluoride. The labels used in ref 39 are kept for easier connection with this work.

manifested through deshielding of the nickel-bonded ^{19}F SSNMR isotropic chemical shifts (δ_{iso}), as has been reported in solution with organic XB donors.[34−38] Comparisons between solid-state and solution NMR indicated that NiF···I(C) halogen bond leads to a deshielding of 25−29 ppm ($\Delta\delta_{iso}$, Figure 1). This deshielding is caused essentially by the XB effect since 3F showed almost the same chemical shift in the solid state and in solution.

The NMR chemical shift anisotropy, represented by the chemical shift tensor (CST), can be used to understand the effect of the XB on δ_{iso}. The principal components of the CST (δ_{11}, δ_{22}, δ_{33} with $\delta_{11} \geq \delta_{22} \geq \delta_{33}$) have been shown to be

controlled mainly by the paramagnetic terms, which themselves can be understood on the basis of the couplings between occupied and vacant molecular orbitals (MOs) having contributions on the NMR active atom and its immediate environment. This analysis has provided valuable insight into the electronic structure of various molecules and their reactivity,[43−54] but studies of halogen-bonded systems are rare. A pioneer example is the analysis of the ^{13}C NMR shielding tensor of the C−I bond in diiodoacetylene acting as XB donor with amines,[55] where the observed and calculated deshielding at the iodine-bonded carbon was traced back to a contribution from the paramagnetic coupling of the occupied π MOs of the alkyne with the vacant $\sigma^*_{C−I}$ MO. Later, a theoretical analysis of halide quadrupolar coupling tensors also pointed to the key role of $\sigma^*_{C−I}$ on the XB acceptor.[30] The chemical shift of ^{15}N NMR of pyridine acting as a XB acceptor was also interpreted qualitatively by the variation in the energy of the occupied and vacant MOs of pyridine under the influence of the XB.[56]

Preliminary nonrelativistic (NR) calculations using a model complex of 1pF halogen-bonded to IC$_6$F$_5$ gave ^{19}F NMR resonances in reasonable agreement with the experimental data.[39] The main effect of the XB is the deshielding of δ_{33}, which in turn is the most shielded component of the CST. The variation in δ_{33} component follows the F···I distance qualitatively and mirrors the variation in δ_{iso}. Nevertheless, a detailed analysis of the CST was not carried out; neither is the ranking of the principal components of the CST understood nor is the effect of the XB on them. In this work, we will fill this gap in knowledge.

■ RESULTS AND DISCUSSION

Structural Features. The reported crystal structures of 1pF and 1oF reveal, respectively, linear or zigzag chains, linked by XBs (Figure 2 and Tables S1−S3 for a representation of the
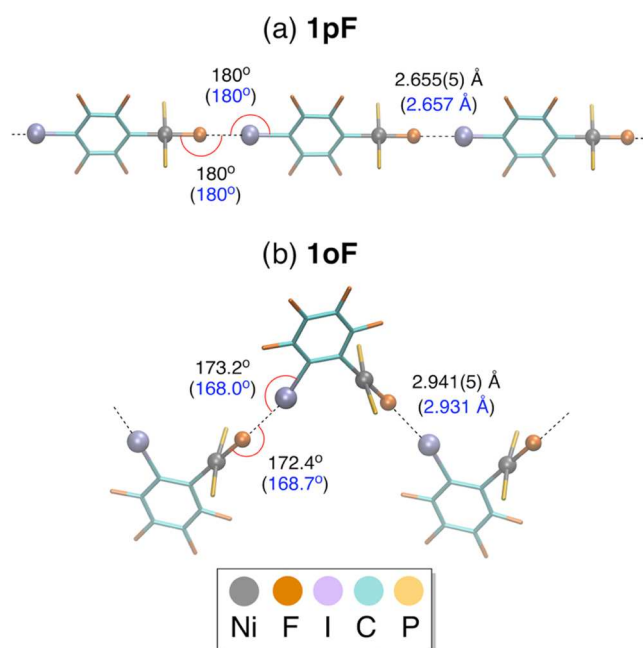

Figure 2. Selected XB structural features for (a) 1pF and (b) 1oF (ethyl groups of the PEt$_3$ ligands perpendicular to the aryl plane omitted), from X-ray diffraction analysis in black,[39] and from calculations with periodic lattice models in blue (this work).

unit cells). The XB environment is similar in the two complexes containing a nickel fluoride as the XB acceptor and a coordinated C_6F_4I ligand as the XB donor. The C−I···F and Ni−F···I angles of **1pF** are perfectly linear (Figure 2a), the first one being consistent with typical XB behavior. This preference for a linear arrangement is also observed for **1oF**, as shown by the C−I···F and Ni−F···I angles of 173.2(2) and 172.4(3)°, respectively (Figure 2b). Note that the NiF···I(C) XB distance is significantly shorter for **1pF**, 2.655(5) Å, than for **1oF**, 2.941(5) Å. On the other hand, **3F** itself, which has no iodine on the aryl ligand, does not form a XB. The Ni−F bond distance of 1.838(6) Å in **3F** resembles that in **1pF** (1.837(5) Å) and **1oF** (1.841(5) Å). Likewise, the plane of the aryl C_6F_4I or C_6F_5 ligand is almost perpendicular to the Ni plane in the three complexes, as shown by the dihedral angles of 85.2(2)° in **1pF**, 84.4(2)° in **1oF**, and 89.2(2)° in **3F**.[39,42]

Several models were used in this study and their associated labeling is given in Scheme 1. Periodic lattice models were

Scheme 1. Nomenclature Used in This Study[a]
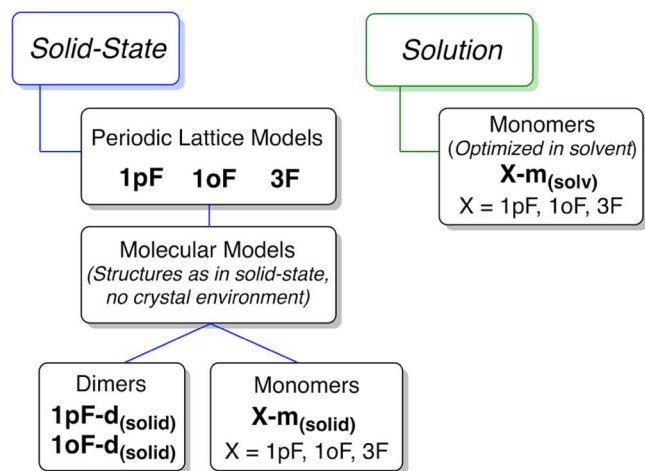
[a]The experimental systems are also labeled **1pF**, **1oF**, and **3F**, as in the original article.[39]

used to include a full representation of the crystalline solid in **1pF**, **1oF**, and **3F**. The benchmark study shows the computed (a, b, c) unit-cell parameters in reasonable agreement with the experimental data, with root-mean-square deviations (RMSDs) of up to 0.43 Å (Tables S1−S3). All functionals considered exhibit similar results, although the unit-cell parameters are slightly better reproduced including the Grimme's dispersion D3 correction[57] (see the Supporting Information, SI). However, the PBE0/pob_TZVP[58] level provides the best reproduction of the structural parameters for the three nickel complexes (Tables S4−S6). In particular, this level of theory

accurately reproduces the NiF···I(C) XB distances; the calculated NiF···I(C) XB lengths of 2.657 and 2.931 Å for **1pF** and **1oF**, respectively, are only 0.002 and 0.010 Å longer than in the experiment, within the limits of 3 standard deviations (conventionally taken as significance limits) (Figure 2). Hence, the significantly shorter XB interaction for **1pF** compared to **1oF** is correctly reproduced. The calculated Ni−F bond distances of **1pF** and **3F** are also well within 3 standard deviations of the experimental data; (calc/exp in Å), **1pF**: 1.848/1.837(5); **3F**: 1.839/1.838(6). The largest difference was found for **1oF** (1.858/1.841(5), difference 0.017 Å, compare 3 standard deviations = 0.015 Å), although the angles describing the zigzag structure of this system were correctly reproduced. Globally, the optimizations using periodic lattice models reproduced correctly the intra- and intermolecular features of the halogen-bonded nickel−fluoride complexes.

^{19}F NMR Chemical Shift Calculations in the Solid State. *Periodic Lattice Models.* The NMR chemical shifts and CST principal components for the nickel-bound fluorine in **1pF**, **1oF**, and **3F** were calculated under periodic boundary conditions using the GIPAW method (see the Computational Methods section for further information).[59] As shown in Table 1, the isotropic chemical shifts (δ_{iso}) are in good agreement with the experimental data, with a maximum deviation of 10 ppm. Moreover, the calculations reproduce the observed chemical shift of the fluoride in the order **1pF** > **1oF** > **3F**. At a qualitative level, the large anisotropy of the CSTs is correctly described, although at a quantitative level, the calculated δ_{11} and δ_{22} are too deshielded and δ_{33} too shielded relative to experiment. This led to calculated span (Ω) and skew (κ) parameter values that are larger than those observed experimentally (Table 1). Nonetheless, the trends in Ω and κ for the three complexes are correctly reproduced. Furthermore, the three components are attributed without ambiguity, with δ_{11}, δ_{22}, and δ_{33} around −150, −300, and −700 ppm, respectively.

Molecular Models. To estimate the influence of the crystal environment on the NMR signature of the nickel-bound fluoride, we studied molecular species having the same structure as in the crystal, but deprived of the crystal environment. Dimeric models of **1pF** and **1oF**, containing a single NiF···I(C) halogen bond, were thus extracted from the structures optimized with periodic lattice models and not further optimized. These species are labeled as **1pF-d$_{(solid)}$** and **1oF-d$_{(solid)}$** (Figure 3). The isotropic ^{19}F NMR chemical shifts and CST principal components for **1pF-d$_{(solid)}$** and **1oF-d$_{(solid)}$** were calculated in the gas phase and compared with the values obtained from the periodic lattice models. In addition, we use these models for the analysis of the relativistic effects using both two- and four-component approaches (2c-ZORA and 4c-

Table 1. Experimental and Calculated ^{19}F SSNMR CST Principal Components (in ppm) for 1pF, 1oF, and 3F Using the Nonrelativistic GIPAW Method

complex	experimental δ (ppm)						calculated[a] δ (ppm)					
	δ_{iso}	δ_{11}	δ_{22}	δ_{33}	Ω[b]	κ[c]	δ_{iso}	δ_{11}	δ_{22}	δ_{33}	Ω[b]	κ[c]
1pF	−359.8(2)	−165	−266	−645	480	0.58	−350.2	−135	−222	−694	558	0.69
1oF	−373.0(2)	−143	−302	−673	530	0.40	−371.5	−107	−270	−738	631	0.48
3F	−393.9(2)	−154	−298	−729	575	0.50	−393.4	−141	−233	−806	665	0.72

[a]Values calculated using the GIPAW method. See the Computational Methods section for more details. [b]Ω calculated span of the chemical shift anisotropy, $\Omega = \delta_{11} - \delta_{33}$. [c]Calculated skew, $\kappa = 3(\delta_{22} - \delta_{iso})/(\delta_{11} - \delta_{33})$.
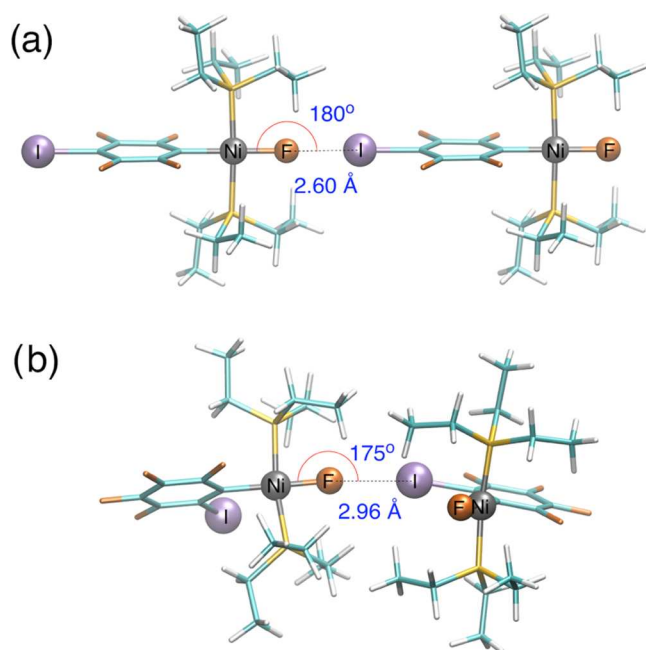
Figure 3. Dimer models (a) **1pF-d**$_{(solid)}$ and (b) **1oF-d**$_{(solid)}$ extracted from the structures optimized with periodic lattice models. The NiF···I(C) halogen bond is indicated by a dashed line. See Tables S4 and S5 for full structural information.

DKS) to represent the spin−orbit coupling (see the Computational Methods section for more details).

As shown in Table S7, all selected methods qualitatively capture the order of chemical shifts observed experimentally. The largest deviation was found for the nonrelativistic approach, with RMSD values of 53.0 (**1pF-d**$_{(solid)}$) and 48.9 (**1oF-d**$_{(solid)}$) ppm. We note that the inclusion of relativistic effects using two- or four-component approaches has little effect on the chemical shifts. The 2c-ZORA level showed RMSD values of 43.1 (**1pF-d**$_{(solid)}$) and 39.4 ppm (**1oF-d**$_{(solid)}$), while the 4c-DKS exhibited RMSD values of 36.8 (**1pF-d**$_{(solid)}$) and 38.8 ppm (**1oF-d**$_{(solid)}$). Hence, the 2c-ZORA level represents a good compromise, and the 4c-DKS gives the smallest deviations by a small margin. Furthermore, the largest systems (114 atoms) are accessible to the 2c-ZORA method, while the computational effort would be significant using 4c-DKS. In addition, the nonrelativistic calculations using either the periodic lattice models or the dimer models gave similar RMSD values and fairly good agreement with the observed values. Thus, intermolecular interactions in the crystal beyond the XB within the dimer have little effect on the NMR signatures. This allows us to use the dimeric models combined with the 2c-ZORA level for further analysis of the ^{19}F SSNMR resonances.

^{19}F NMR Chemical Shift Calculations for Solvated Complexes. The modeling of the ^{19}F NMR chemical shifts in solution was carried out using the monomeric nickel−fluoride complexes where no XB is formed, named **1pF-m**$_{(solv)}$, **1oF-m**$_{(solv)}$, and **3F-m**$_{(solv)}$. These species were optimized in benzene solution using the PBE0 functional and the implicit SMD solvation model[60] (Table S9). The results show that the structural features of the complexes in solution are globally similar to those in the solid state. However, the Ni−F bond distance calculated in solution is significantly shorter (1.828 Å in **1pF-m**$_{(solv)}$) than the one calculated with a periodic lattice

model (1.848 Å in **1pF**). The C−I bond distance calculated in solution is also slightly shorter than in the solid state. In addition, the Ni−C(aryl) bond length for **1oF** is longer than in **1oF-m**$_{(solv)}$, which could be due to some strain in the zigzag structure adopted in the solid state.

The ^{19}F NMR chemical shifts in solution calculated at the 2c-ZORA-PBE/TZ2P level[61−68] are in very good agreement with the experimental data, except for **1oF-m**$_{(solv)}$ that was calculated to be ~23 ppm more shielded than in the experiment (see $\Delta\delta$, Table 2). The lack of inclusion of

Table 2. Experimental and Calculated (NR and 2c-ZORA) ^{19}F NMR Chemical Shifts (δ) (in ppm) for 1pF-m$_{(solv)}$, 1oF-m$_{(solv)}$, and 3F-m$_{(solv)}$ in Benzene Solution

complex	exp[a]	calculations in benzene solution[c]			
		NR (δ)	$\Delta\delta$[b]	2c-ZORA (δ)	$\Delta\delta$[b]
1pF-m$_{(solv)}$	−388.3	−390.5	−2.2	−388.4	−0.1
1oF-m$_{(solv)}$	−397.9	−421.1	−23.2	−420.8	−22.9
3F-m$_{(solv)}$	−394.3	−396.5	−2.2	−396.4	−2.1

[a]Values as reported in ref 39. [b]$\Delta\delta = \delta$(calc) − δ(exp). [c]See the Computational Methods section.

dynamics and explicit solvent effects on NMR could bias these results, especially in the case of **1oF-m**$_{(solv)}$. For instance, the influence of the *ortho* iodine on the fluoride resonance, which could depend significantly on the libration of the aryl group, is unlikely to be properly represented by the single structure retained for the calculation. It should be noted that the calculated chemical shifts using nonrelativistic (NR) are within a few ppm of 2c-ZORA calculations, indicating again that relativity has little effect on the ^{19}F NMR chemical shifts in these species.

Calculation of the NMR Signatures of the XB. In this work, we were particularly interested in an estimation of the NMR signatures of the XB for the nickel-bound fluoride, which is given by the difference in δ_{iso} between solid-state and solution NMR.[39] Therefore, we analyzed the chemical shifts of the systems involved and not involved in the XB using the 2c-ZORA approach. The dimeric **1pF-d**$_{(solid)}$ and **1oF-d**$_{(solid)}$ species extracted from the structures optimized with periodic lattice models (Figure 3) were selected to represent the δ_{iso} in the solid state, while the monomers **X-m**$_{(solv)}$ (X = **1pF**, **1oF**, and **3F**) optimized in benzene solution were selected to represent the δ_{iso} in solution. Additionally, we introduced here the corresponding monomeric species extracted also from the structures optimized with periodic lattice models, named **X-m**$_{(solid)}$, where X = **1pF**, **1oF**, and **3F** (see Table S8 for full information on the calculated NMR resonances).

The observed and calculated ^{19}F NMR signatures for **1pF**, **1oF**, and **3F** systems are shown in Table 3. The deshielding of the nickel-bonded fluorine in the presence of the XB and its order of magnitude is well reproduced for **1pF** (see $\Delta\delta_{iso}$, Table 3). Likewise, the results also nicely reproduce the fact that **3F** has essentially the same chemical shift in the solid state and in solution. On the other hand, a discrepancy appears in the NMR signature for **1oF** since the δ_{iso} of the monomer in solution (**1oF-m**$_{(solv)}$) is not correctly reproduced (exp 24.9 vs calcd 47.5 ppm). Nevertheless, this chemical shift variation improves when comparing with **1oF-m**$_{(solid)}$ (calcd 21.9 ppm). Using the monomeric species as reference also improve the agreement between experimental and calculated effects of the XB in the case of **1pF**. The sole mismatch in the case of **1oF**

Table 3. Experimental and Calculated (2c-ZORA) ^{19}F NMR Chemical Shifts (in ppm) for the Halogen-Bonded Dimers 1pF-d$_{(solid)}$ and 1oF-d$_{(solid)}$, the Monomeric Species X-m$_{(solid)}$, and the Monomers X-m$_{(solv)}$ in Benzene Solution, Where X = 1pF, 1oF, and 3F

	experimental δ_{iso}			calculated δ_{iso} (molecular models)			calculated δ_{iso} (solution)	
X	solid state	solution	$\Delta\delta_{iso}$ [a]	dimer X-d$_{(solid)}$	monomer X-m$_{(solid)}$	$\Delta\delta_{iso}$ [b]	monomer X-m$_{(solv)}$	$\Delta\delta_{iso}$ [c]
1pF	−359.8(2)	−388.3	28.5	−356.7	−387.9	31.2	−388.4	31.7
1oF	−373.0(2)	−397.9	24.9	−373.3	−395.2	21.9	−420.8	47.5
3F	−393.9(2)	−394.3	0.4	NA [e]	−398.1	NA [e]	−396.4	−1.7 [d]

[a]Calculated as $\Delta\delta_{iso} = \delta_{iso}$ (solid) − δ_{iso} (solution). [b]Calculated as the difference between X-d$_{(solid)}$ and X-m$_{(solid)}$. [c]Calculated as the difference between X-d$_{(solid)}$ and X-m$_{(solv)}$. [d]Calculated as the difference between 3F-m$_{(solid)}$ and 3F-m$_{(solv)}$. [e]Not applicable.

points out the possible importance of the structural features of the species in solution and the need for including dynamics and specific solvent effects, as already noted in previous NMR studies.[69−71]

Effect of the XB on the Chemical Shift Tensor. To understand the origin of deshielding at the nickel-bound fluoride upon XB, we compared the chemical shift tensors (CSTs) in (1pF/1oF)-m$_{(solid)}$ and (1pF/1oF)-d$_{(solid)}$. In this way, this deshielding can be exclusively attributed to the XB interaction. For comparison, 3F-m$_{(solid)}$ has been included as a representative species that does not become involved in a XB. The calculated principal components and the orientation of the principal axes of the ^{19}F SSNMR CST are shown in Table 4 for

Table 4. Calculated (2c-ZORA) ^{19}F SSNMR CST Principal Components (in ppm) of 1pF-d$_{(solid)}$, 1oF-d$_{(solid)}$, and 3F-m$_{(solid)}$ [a]

	calculated δ (ppm)			
species	δ_{iso}	δ_{11}	δ_{22}	δ_{33}
1pF-d$_{(solid)}$	−356.7	−143.7	−223.7	−702.8
1pF-m$_{(solid)}$	−388.0	−101.7	−245.6	−816.7
$\Delta\delta_{ii}^{d-m}$	31.3	−42.0	21.9	113.9
1oF-d$_{(solid)}$	−373.3	−118.9	−271.9	−729.2
1oF-m$_{(solid)}$	−395.2	−97.4	−288.8	−799.4
$\Delta\delta_{ii}^{d-m}$	21.9	−21.5	16.9	70.2
3F-m$_{(solid)}$	−398.2	−152.1	−234.4	−808.0

[a]The orientations of the principal axes of the CST are shown at the top with red, green, and blue arrows corresponding to δ_{11}, δ_{22}, and δ_{33}. The experimental values are given in Table 1.

monomers and dimers. All species have identical orientations of the principal axes of the CST and identical ranking of the principal components: the most deshielded component (δ_{11}) is along Ni−F, while the most shielded one (δ_{33}) is perpendicular to the Ni coordination plane. This pattern is characteristic of a square-planar Ni^{II}−fluoride complex as can be established by comparison with a model system NiH(F)(PH$_3$)$_2$. The calculated CST values for this species are consistent: same directions of the principal axes and ($\delta_{11} > \delta_{22} \gg \delta_{33}$) in similar regions of the spectra (see Table S11).

The positions of the resonances for the calculated molecular models and the observed crystalline systems are in excellent agreement, as illustrated in Figure 4. The comparison is especially satisfying for δ_{33}, with almost identical observed and
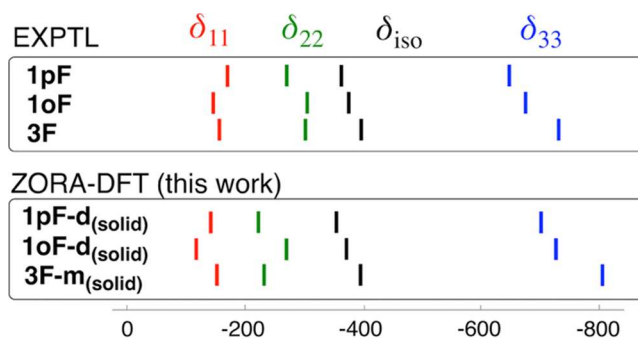
Figure 4. Positions of the ^{19}F SSNMR chemical shift tensor components (in ppm) for (top) experimental 1pF, 1oF, and 3F[39] and (bottom) 2c-ZORA calculations for 1pF-d$_{(solid)}$, 1oF-d$_{(solid)}$, and 3F-m$_{(solid)}$.

calculated variations for 1pF, 1oF, and 3F. The results are also very good for δ_{11}, but some deviation from the experimental values is found in δ_{22}, especially for 1oF-d$_{(solid)}$. For 1pF, this work gives results which are more accurate than in the earlier study,[39] although the observed pattern for this system was already reproduced using a model complex of 1pF halogen-bonded to IC$_6$F$_5$.

The effect of the XB is different for each component: δ_{11} is shielded by the XB by less than 50 ppm; in contrast, δ_{22} and δ_{33} are both deshielded, the main effect being found for δ_{33} with $\Delta\delta_{33}^{d-m}$ of 114 (1pF) and 70 (1oF) ppm (see $\Delta\delta_{ii}^{d-m}$, Table 4). Thus, the deshielding of δ_{iso} with the XB is due to the change of the two principal components that are associated with the principal axes perpendicular to the Ni−F bond, and mainly with the one that is perpendicular to the coordination plane of the complex. Similarly, a simulation of the effect of XB in HF···ICH$_3$ also indicated a deshielding of the components perpendicular to the H−F axis (Table S11 and Figure S2).

Analysis of the ^{19}F NMR Shielding Components. To understand the nature of the CST and its variation upon XB, we considered a simple method for examining the relationship between MOs and CST, based on Ramsey's perturbation equations of nuclear shielding[44,47] (see the Supporting Information for further details). This analysis method has been used successfully for main group atoms of nuclear spin of 1/2, such as carbon, nitrogen, and phosphorus.[43,44,47,50−52] In the following, we use the shielding, σ, rather than chemical shift, δ, since it is the former that is calculated and analyzed. This corresponds to a change of reference ($\delta = \sigma_{ref} - \sigma$) where σ_{ref} is the ^{19}F shielding in CFCl$_3$ (see the Computational Methods section). In a 2c-ZORA scheme, the shielding can be split into diamagnetic (σ^{dia}) and paramagnetic plus spin−orbit (SO) (σ^{p+SO}) contributions. For n = 2 and 3 main group elements, the diamagnetic contribution is usually almost

Table 5. Calculated (2c-ZORA) Shielding Tensor Principal Components for the Monomeric and Dimeric Species, X-m$_{(solid)}$ and X-d$_{(solid)}$, with Diamagnetic σ_{ii}^{dia} and Paramagnetic + Spin−Orbit Contributions σ_{ii}^{p+SO} (in ppm)

| species	σ_{iso}	σ_{11}	σ_{22}	σ_{33}	σ_{11}^{dia}	σ_{22}^{dia}	σ_{33}^{dia}	σ_{11}^{p+SO}	σ_{22}^{p+SO}	σ_{33}^{p+SO}
1pF-m$_{(solid)}$	537.6	251.3	395.2	966.3	482.8	455.3	446.6	−231.4	−60.2	519.7
1pF-d$_{(solid)}$	506.3	293.3	373.3	852.4	494.8	455.9	447.7	−201.4	−82.6	404.5
$\Delta\sigma_{ii}^{d-m}$	−31.3	42.0	−21.9	−113.9	12.0	0.6	1.1	30.0	−22.4	−115.2
1oF-m$_{(solid)}$	544.8	247.0	438.4	949.0	481.2	455.3	446.7	−234.1	−16.9	502.2
1oF-d$_{(solid)}$	522.9	268.5	421.5	878.8	489.2	453.9	444.9	−220.7	−32.4	433.9
$\Delta\sigma_{ii}^{d-m}$	−21.9	21.5	−16.9	−70.2	8.0	−1.4	−1.8	13.4	−15.5	−68.3

isotropic.[39−44] This is less the case for fluorine in the present complexes, where σ_{11}^{dia} is about 40 ppm more shielding than σ_{22}^{dia} and σ_{33}^{dia} (Table 5). However, the differences between σ_{11}, σ_{22}, and σ_{33} are much larger in the σ^{p+SO} terms, as illustrated by the difference of over 700 ppm between σ_{11}^{p+SO} and σ_{33}^{p+SO} for both **1pF-m$_{(solid)}$** and **1oF-m$_{(solid)}$** systems. Thus, as was found for other nuclei such as carbon,[72−78] it is sufficient to consider only the σ^{p+SO} term to probe the origin of the anisotropy of the shielding tensor. Furthermore, the spin−orbit part in σ^{p+SO} is small as previously shown by the equivalence in the chemical shifts calculated with NR and 2c-ZORA methods. It is thus possible to focus on the paramagnetic part of the shielding.

We now analyze the σ_{ii}^{p+SO} terms. To interpret these terms, Zilm et al. used an orbital "rotation" model in the case of atomic p orbitals and stated that "The paramagnetic terms arise from the interaction of occupied orbitals with virtual orbitals that are rotated by 90° and may lead to either deshielding or shielding. The normal interaction leads to deshielding."[79] In this work, it is helpful to consider first the cases of H−F and Cl−F, before presenting the nickel−fluoride complexes.

In H−F, which is aligned with the x axis, the large negative (deshielding) paramagnetic terms in the direction perpendicular to H−F (y or z) can be traced back to contributions from the paramagnetic coupling of the F 2p$_z$ (or 2p$_y$) lone pairs (LPs) with the vacant σ_{H-F}^{*} MO via the $\hat{l}_y$ (or $\hat{l}_z$) angular momentum operator, as shown in Scheme 2a (see the Supporting Information for further details). In contrast, there is no vacant orbital to couple paramagnetically with either of these F 2p$_y$ or 2p$_z$ LPs via the $\hat{l}_x$ angular momentum operator. Consequently, the most shielded term is along H−F and the directions perpendicular to H−F are deshielded.

In Cl−F, the F is shielded relative to the anionic F$^-$.[80] Cornwell showed that this arises from the magnetic interaction of the out-of-phase combination of Cl 3p and F 2p LPs with the vacant σ_{Cl-F}^{*} orbital.[81] As part of their general interpretation, Zilm et al. pointed out the effect of p orbitals on neighboring atoms: "when two p orbitals in an occupied MO have opposite phase, the dominant interaction will lead to deshielding but the other atom will be shielded." Thus, in Cl−F, Cl is deshielded and F shielded.[79] The occupied and vacant MOs involved in the paramagnetic shielding at F are shown schematically in Scheme 2b. Since the only vacant orbital is σ_{Cl-F}^{*}, there is no paramagnetic term along the Cl−F direction. As a result, the most shielded directions for F in Cl−F are perpendicular to the molecular axis (see the Supporting Information for further details). Related findings have been obtained to account for the effect of substituents in a set of aliphatic fluorides.[82]

Case of the Square-Planar Nickel−Fluoride Monomer. A similar analysis to that for Cl−F can be applied to the nickel−fluoride complexes, keeping in mind that the orbital rotation

Scheme 2. Illustration of the Sign of the Paramagnetic Coupling of Occupied to Vacant Orbitals at F Using the Orbital Rotation Model Applied to the Representative Cases (a) H−F and (b) Cl−F;[79] All Orbitals Are Drawn Schematically with a Focus on Their Topology
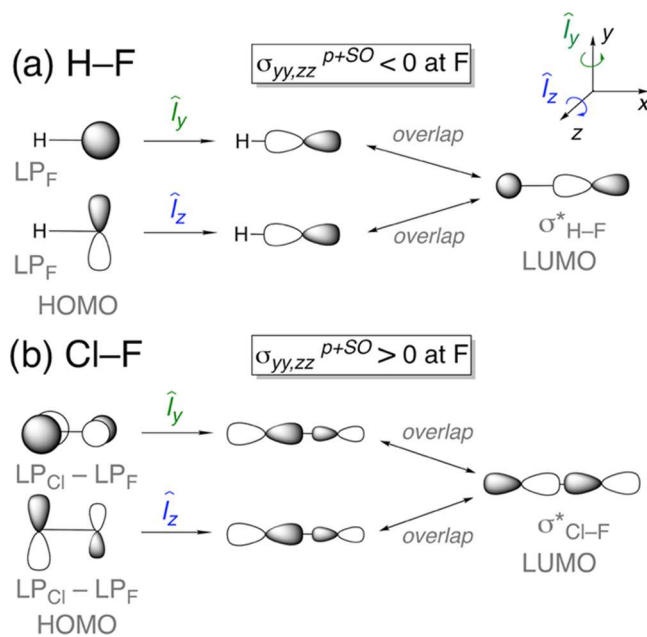
model applied to the metal d orbitals does not always correspond to 90° rotation.[83] In the present case, 45 and 90° rotations will be used; a full description of the action of angular momentum operators on all d orbitals can be found in ref 46. As shown in Scheme 3, the fluorine 2p$_y$ and 2p$_z$ LPs perpendicular to the Ni−F axis are engaged in four-electron interaction with occupied Ni (3d$_{xy}$ and 3d$_{xz}$) and Ni−P orbitals. Consequently, the out-of-phase combinations of these Ni 3d (or Ni−P bonding) and symmetry-adapted F 2p orbitals are occupied and all out-of-phase occupied orbitals have larger coefficients on Ni (or Ni−P) than on F due to the high electronegativity of fluorine. Thus, in all cases, the coupling of these occupied orbitals with the vacant σ_{Ni-F}^{*} orbital via the appropriate angular momentum operator ($\hat{l}_z$ or $\hat{l}_y$) leads to shielding at the fluorine. Note that the action of $\hat{l}_z$ or $\hat{l}_y$ on Ni (3d$_{xy}$ or 3d$_{xz}$) gives Ni (3d$_{x^2-y^2}$ or 3d$_{z^2-x^2}$) atomic functions, respectively. Both of the orbitals overlap significantly with σ_{Ni-F}^{*}, which has a strong Ni 3d$_{x^2-y^2}$ character.[46] This accounts for the large shielding influence of Ni at F in the z (δ_{33}) and y (δ_{22}) directions, respectively. Furthermore, there are more occupied orbitals (with Ni center and the Ni−P bonding character) in the xy plane of the square-planar complex than in the perpendicular xz plane. Therefore, fluorine is more shielded perpendicular to the Ni coordination plane, i.e.,

Scheme 3. Coupling of Occupied Ni (or Ni-Phosphine)/Fluorine 2p Lone Pairs *via* the Angular Momentum Operator and Their Contribution to the Paramagnetic Term in the *trans*-[NiF(2,3,5,6-C$_6$F$_4$I)(PEt$_3$)$_2$] Complex[a]
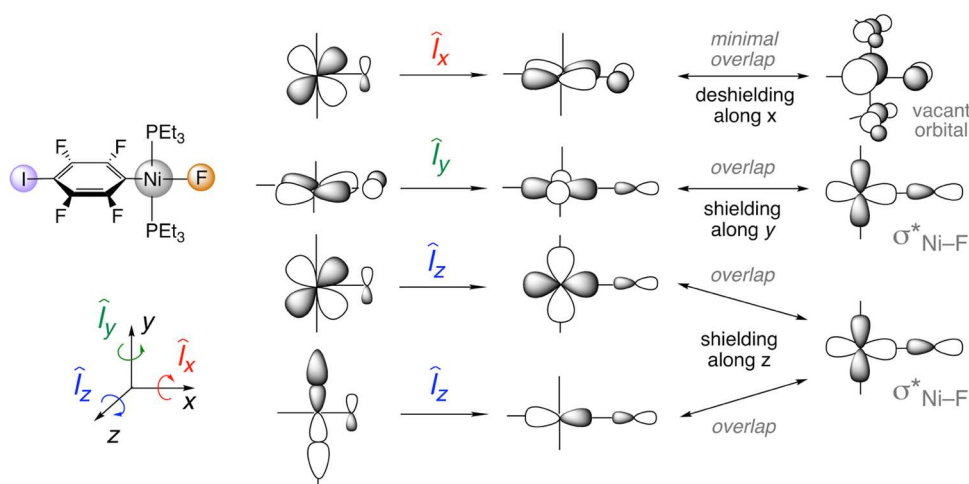
[a]All orbitals are drawn schematically with a focus on their topology.

along the z axis (δ_{33}). In contrast, the shielding influence of Ni at F along x (the Ni−F direction) is almost nil. Indeed, the paramagnetic term along x comes in good part from the coupling via the $\hat{l}_x$ angular momentum operator of the occupied Ni 3d$_{xy}$ − F 2p$_y$ orbital with a high-lying vacant orbital having large Ni 4p$_z$ and $\sigma^*_{P−C}$ and small F 2p$_z$ characters (Scheme 3).[84] The action of $\hat{l}_x$ on Ni 3d$_{xy}$ gives Ni 3d$_{xz}$,[46] and thus the overlap at Ni between the rotated occupied and the vacant orbital is nil. Only a fluorine deshielding contribution remains, but it is small because the vacant orbital is at high energy. An NLMO analysis[45,46] supports the presented qualitative orbital rotation model (Table S13).

As a consequence of these various effects, the most deshielded direction is along Ni−F and the directions perpendicular to Ni−F are shielded especially the one perpendicular to the coordination plane. A similar interpretation of the shielding role of the occupied d orbitals of the metal was given for interpreting the isotropic ^{19}F chemical shift in a cobalt−fluorine complex.[41]

Case of the Halogen-Bonded Nickel−Fluoride Dimer. To understand the effect of the XB on the NMR spectra, we first carried out an energy decomposition analysis of the self-assembled nickel complexes considering **X-d$_{(solid)}$** and **X-m$_{(solid)}$** (X = **1pF** and **1oF**) to obtain some information on the energetics. We use the variational EDA[85,86] based on absolute localized molecular orbitals[87,88] (ALMO-EDA), which reveals that the interactions between these neutral inorganic species are qualitatively similar to that found for the charged halogen-bonded organic species CX$_3$I···Y$^−$ (X = F, Cl, Br and I; Y = F, Cl and Br).[14] The noticeable result is that the total interaction energy is 17.7 and 8.7 kJ mol^{-1} for **1pF** and **1oF**, respectively, suggesting that the neutral nickel-bonded fluoride is a good XB acceptor toward the C−I bond of the iodoaryl ligand acting as XB donor. Although no experimental values of these interaction energies in the solid are available, they are of the expected order of magnitude for XBs. The ALMO-EDA study shows that the largest attractive term derives from the permanent electrostatics but that it is offset by the even larger Pauli repulsion. Thus, in these neutral nickel complexes, the stabilizing polarization and charge transfer terms contribute together with permanent electrostatics to the attraction

between the two monomeric complexes (see Table S12 for further details).

We now turn our attention to the characteristics of the ^{19}F NMR shielding tensor in **1pF-d$_{(solid)}$** and **1oF-d$_{(solid)}$**, relative to that in **1pF-m$_{(solid)}$** and **1oF-m$_{(solid)}$**, respectively (Table 5). As we mentioned before, the major changes between the halogen-bonded dimer and the corresponding monomer are mostly contained in a deshielding of the σ_{33} component (Tables S13 and S14). We recall that the paramagnetic term is inversely proportional to the energy gap between the occupied and vacant orbitals linked by the angular momentum operator. Our calculations show an increase in the energy gap in the dimer relative to the monomer for the main pair of MOs involved in the shielding, notably Ni 3d$_{xy}$ − F 2p$_y$ and $\sigma^*_{Ni−F}$ (Scheme 3). This change allows a simple interpretation of the decrease of the paramagnetic term σ_{33}^{p+SO}, and consequent reduction in shielding. The lowering of the energy of the occupied orbital upon formation of the XB is a direct consequence of the bonding interaction between the two systems. It should be noted though that the bonding interaction involves mostly orbitals along the Ni−F and I−C bonds, but lowering of other orbitals is also expected. The lowering of the lowest unoccupied molecular orbital (LUMO) is more difficult to estimate but is systematically seen in all models of halogen-bonded systems considered. Further studies with a wider set of metal−fluoride complexes[89] and non-metallic fluorine species are currently underway to extend the interpretation presented in this work. In addition, it is not yet possible to elaborate on the existence or lack of relationship between the energetics of the XB and its NMR signature. For this, we also need to study a larger set of systems. One can however remark that mostly orbitals co-axial with the XB are involved in its strength, while NMR shielding is based on the contribution of occupied orbitals perpendicular to the XB direction and empty co-axial orbitals. Since different orbitals are involved in the two phenomena, the nature of relationship cannot be established from this work.

■ CONCLUSIONS

The effect of the XB on the ^{19}F SSNMR chemical shift was demonstrated in a previous study by comparing the NMR

spectra of *trans*-[NiF(2,3,5,6-C$_6$F$_4$I)(PEt$_3$)$_2$] **1pF** and *trans*-[NiF(2,3,4,5-C$_6$F$_4$I)(PEt$_3$)$_2$] **1oF** complexes,[39] with that of a complex incapable of XB formation, *trans*-[NiF(C$_6$F$_5$)(PEt$_3$)$_2$] **3F**.[42] For **1pF** and **1oF**, the presence of the XB is manifested through deshielding of the nickel-bound ^{19}F SSNMR isotropic chemical shifts (δ_{iso}), relative to values obtained in solution, where no XB is observed.[39] The present work has used a computational protocol to provide insight into the specificities of the ^{19}F chemical shift resonances in square-planar nickel−fluoride complexes involved and not involved in a XB situation.

The average chemical shift δ_{iso} and also the ranking of the principal components δ_{11}, δ_{22}, and the strongly shielded δ_{33} are well reproduced for the nickel-bonded fluoride with 2c-ZORA calculations for a halogen-bonded dimer model. This dimer model is extracted from the structures optimized with periodic lattice models, which themselves are in good agreement with experiment. This result indicates that the XB has a significant effect but the crystal packing has no visible influence on the fluoride chemical shifts of these complexes. The analysis of relativistic effects also indicates that the ^{19}F NMR resonances are well reproduced with the 2c-ZORA Hamiltonian, although agreement improves with the four-component Dirac−Kohn−Sham approach. In general, the agreement with experiment is better for **1pF** than for **1oF**.

Comparison between the calculated ^{19}F chemical shifts (isotropic and principal components) of the isolated monomeric square-planar complexes and the corresponding halogen-bonded dimers provides the change in the NMR resonances due to the XB. These calculated shifts are in good agreement with the observed values, evaluated as the differences between the resonances in solution, where XB is absent and that in the solid state, where it is present. In particular, the calculations reproduce nicely the downfield shift of δ_{iso} on forming the XB driven mostly by the change in δ_{33} with an additional contribution from δ_{22}.

We used the orbital rotation model to analyze the paramagnetic terms of three principal components of the ^{19}F CST in the monomeric nickel−fluoride complex. The paramagnetic terms, come from the coupling *via* the angular momentum operator of occupied and vacant orbitals. In these square-planar complexes, they involve the F 2p lone pairs combined in an antibonding way with the symmetry-adapted Ni and Ni−P occupied orbitals and the vacant $\sigma^*_{Ni−F}$ orbital, essentially the LUMO (Ni d$_{x^2−y^2}$). As exemplified by Zilm et al. for the emblematic Cl−F,[79] the paramagnetic term is positive, and thus shielding increases at fluorine in the directions perpendicular to the axis since the Cl/F out-of-phase highest occupied orbital is dominated by chlorine. In the nickel complexes, the Ni or Ni−P character dominates in the Ni/F out-of-phase highest occupied orbitals and thus induces a shielding at fluorine in the direction perpendicular to the Ni−F axis. Since there are more Ni/F occupied antibonding orbitals in the coordination plane than out of it, the most shielded direction is perpendicular to the coordination plane. The least shielded direction δ_{11}, which is along Ni−F, involves occupied and vacant orbitals perpendicular to the Ni−F axis. However, the Ni shielding contribution at F is essentially nil because of the lack of overlap at Ni between the two coupled orbitals which have 3d and 4p characters, respectively. We show that these features are characteristic of square-planar nickel−fluoride complexes.

In the halogen-bonded nickel−fluoride systems, the positive paramagnetic terms at F in the δ_{22} and δ_{33} components are

decreased. A rationale for this is that the occupied-vacant energy gap between orbitals involved in the shielding increases on forming the XB as a direct consequence of the bonding interaction. The generality of this interpretation needs to be assessed by the study of a wider range of metal-bound fluoride complexes.

■ COMPUTATIONAL METHODS

Structure Optimization. *Calculations with Periodic Lattice Models.* **1pF**, **1oF**, and **3F** were optimized at the density-functional theory (DFT) level using periodic boundary conditions, as implemented in *CRYSTAL-17*.[90,91] The X-ray diffraction data[39,42] were employed to generate the initial unit-cell parameters and atomic positions. The experimentally observed symmetry of the crystal lattices has been maintained during structural optimizations. The performance of the PBE0[92] and HSE06[93] functionals and the inclusion of Grimme's dispersion D3 correction[57] in reproducing the solid-state structures was assessed. Stuttgart−Dresden relativistic pseudopotentials with the associated Gaussian-type basis sets were employed for Ni, I, and P; the pob_TZVP_rev2[58] basis set for the rest of the atoms (F, C, H). Calculations used a Monkhorst−Pack k-points mesh of 6 × 4 × 4 (**1pF**), 4 × 4 × 4 (**1oF**), and 4 × 4 × 2 (**3F**). It appeared that the inclusion of dispersion D3 correction was not beneficial to the reproduction of structural parameters that are important for the NMR shielding calculations, even if it was beneficial for the unit-cell parameters. The PBE0 functional that best reproduced features essential to the NMR study was thus selected.

Calculations for Solvated Complexes. The three monomeric nickel−fluoride complexes, named **1pF-m$_{(solv)}$**, **1oF- m$_{(solv)}$**, and **3F-m$_{(solv)}$**, were optimized using the *Gaussian* software,[94] including the implicit SMD solvation model[60] for benzene. These calculations were carried out using the PBE0 functional combining a Stuttgart−Dresden relativistic pseudopotential with its associated basis set for Ni, the aug-pcSseg-2[95] basis set for F, and pcseg-2[96] basis sets for the rest of the atoms.

^{19}F NMR Chemical Shift Calculations in the Solid State. *Periodic Lattice Models.* The NMR chemical shifts and chemical shift tensor components for the nickel-bound fluorine in **1pF**, **1oF**, and **3F** were computed with the gauge-including projector augmented wave (GIPAW) method,[59] as implemented in the *Quantum Espresso*[97] software (ver. 7.1). Calculations used a Monkhorst−Pack k-point grid of 6 × 4 × 4 (**1pF**), 4 × 4 × 4 (**1oF**), or 4 × 4 × 2 (**3F**) and a cutoff value for energy was set to 90 Ry.

Molecular Models. The dimeric (**1pF-d$_{(solid)}$** and **1oF-d$_{(solid)}$**) and monomeric (**1pF-m$_{(solid)}$**, **1oF-m$_{(solid)}$**, and **3F-m$_{(solid)}$**) models were extracted from the optimized crystalline systems, without performing any further geometry optimization. The ^{19}F NMR chemical shifts were calculated in gas phase using the PBE functional[64,65] in conjunction with the all-electron Slater-type orbitals (STO) TZ2P basis sets.[67] The calculations were performed including scalar (SR) and spin−orbit (SO) relativistic effects at the two-component (2c) level using the zeroth-order regular approximation (ZORA) Hamiltonian,[61−63,66,68] as implemented in the *ADF* program.[98,99] The gauge-origin dependence was handled using gauge-including atomic orbitals (GIAO) approach.[100]

The 2c-ZORA results for **1pF-d$_{(solid)}$** and **1oF-d$_{(solid)}$** were compared with those obtained by a nonrelativistic (NR) method using *Gaussian* software.[94] The PBE functional was selected, combining a Stuttgart−Dresden relativistic pseudopotential with its associated basis set for Ni, the aug-pcSseg2 basis set for F and pcseg-2 basis sets for the rest of the atoms. Additional calculations were performed using the fully four-component Dirac−Kohn−Sham (4c-DKS) method in combination with the Dirac−Coulomb Hamiltonian,[101,102] as implemented in the *ReSpect* program.[103] The PBE functional was selected combining the all-electron Dyall's VTZ basis sets for Ni, F, and I, and the uncontracted pcS-2[104,105] basis sets for the rest of the atoms. Note that although some minor differences between the NR-PBE, 2c-ZORA, and 4c-DKS approaches can be expected, for example, from the different types of basis sets (Gaussian

vs Slater basis sets), these calculations can be used to evaluate the importance of relativistic effects.

^{19}F NMR Chemical Shift Calculations for Solvated Complexes. The ^{19}F NMR chemical shifts of the monomers in solution (**1pF-m$_{(solv)}$**, **1oF-m$_{(solv)}$**, and **3F-m$_{(solv)}$**) were calculated using the geometries optimized with the SMD solvation model[60] for benzene. These calculations were carried out using the COSMO model for simulating bulk solvation in benzene at the 2c-ZORA-PBE/TZ2P level, implemented in the *ADF* program. The 2c-ZORA results were compared with those obtained by a nonrelativistic (NR) method including the SMD model for solvation in benzene, as implemented in *Gaussian* software. These calculations were obtained using the PBE functional combining a Stuttgart−Dresden relativistic pseudopotential with its associated basis set for Ni, the aug-pcSseg2 basis set for F and pcseg-2 basis sets for the rest of the atoms. All ^{19}F NMR chemical shifts (δ_{iso}) are referenced to trichlorofluoromethane (CFCl$_3$, calculated shielding = 139.0 (NR), 149.6 ppm (2c-ZORA)).

^{19}F NMR Chemical Shift Calculations for H−F, HF···ICH$_3$, and NiH(F)(PH$_3$)$_2$ Species. These species were optimized at the ZORA-PBE0/TZ2P level. Subsequent ^{19}F NMR chemical shift calculations were carried out at the ZORA-PBE/TZ2P level. For HF···ICH$_3$, the XB distance was set equal to that in **1pF-d$_{(solid)}$** (2.657 Å), while the rest of the structural parameters were optimized.

Analysis of the NMR Chemical Shifts and Electronic Structure. Analyses of the bonding and the shielding were carried out with the *NBO 6.0* program.[106,107] Interaction between **X-m$_{(solid)}$** to yield **X-d$_{(solid)}$** for **X** = **1pF** and **1oF** was evaluated with the variational EDA[85,86] based on absolute localized molecular orbitals[87,88] (ALMO-EDA) approach of Head-Gordon, as implemented in the *Q-Chem 5.2* software package.[108] For consistency, the same combination of functional and basis set was used for the NBO and NMR calculations.

A dataset collection of the computational results is available in the *ioChem-BD* repository[109] and can be accessed via https://doi.org/10.19061/iochem-bd-6-189.

ASSOCIATED CONTENT

Supporting Information

The Supporting Information is available free of charge at https://pubs.acs.org/doi/10.1021/acs.inorgchem.2c04063.

Additional computational data and figures (PDF)

Cartesian coordinates (ZIP)

AUTHOR INFORMATION

Corresponding Authors

Abril C. Castro − *Hylleraas Centre for Quantum Molecular Sciences, Department of Chemistry, University of Oslo, 0315 Oslo, Norway;* orcid.org/0000-0003-0328-1381; Email: abril.castro@kjemi.uio.no

Christophe Raynaud − *ICGM, Université Montpellier, CNRS, ENSCM, 34090 Montpellier, France;* orcid.org/0000-0003-0979-2051; Email: christophe.raynaud1@umontpellier.fr

Odile Eisenstein − *Hylleraas Centre for Quantum Molecular Sciences, Department of Chemistry, University of Oslo, 0315 Oslo, Norway; ICGM, Université Montpellier, CNRS, ENSCM, 34090 Montpellier, France;* orcid.org/0000-0001-5056-0311; Email: odile.eisenstein@umontpellier.fr

Authors

Michele Cascella − *Hylleraas Centre for Quantum Molecular Sciences, Department of Chemistry, University of Oslo, 0315 Oslo, Norway;* orcid.org/0000-0003-2266-5399

Robin N. Perutz − *Department of Chemistry, University of York, YO10 5DD York, United Kingdom;* orcid.org/0000-0001-6286-0282

Complete contact information is available at:
https://pubs.acs.org/10.1021/acs.inorgchem.2c04063

Notes

The authors declare no competing financial interest.

REFERENCES

(1) Desiraju, G. R.; Ho, P. S.; Kloo, L.; Legon, A. C.; Marquardt, R.; Metrangolo, P.; Politzer, P.; Resnati, G.; Rissanen, K. Definition of the halogen bond (IUPAC Recommendations 2013). *Pure Appl. Chem.* **2013**, *85*, 1711−1713.

(2) Corradi, E.; Meille, S. V.; Messina, M. T.; Metrangolo, P.; Resnati, G. Halogen Bonding versus Hydrogen Bonding in Driving Self-Assembly Processes. *Angew. Chem., Int. Ed.* **2000**, *39*, 1782−1786.

(3) Aakeröy, C. B.; Fasulo, M.; Schultheiss, N. F.; Desper, J.; Moore, C. Structural competition between hydrogen bonds and halogen bonds. *J. Am. Chem. Soc.* **2007**, *129*, 13772−13773.

(4) Gilday, L. C.; Robinson, S. W.; Barendt, T. A.; Langton, M. J.; Mullaney, B. R.; Beer, P. D. Halogen Bonding in Supramolecular Chemistry. *Chem. Rev.* **2015**, *115*, 7118−7195.

(5) Vioglio, P. C.; Chierotti, M. R.; Gobetto, R. Solid-state nuclear magnetic resonance as a tool for investigating the halogen bond. *CrystEngComm* **2016**, *18*, 9173−9184.

(6) von der Heiden, D.; Vanderkooy, A.; Erdélyi, M. Halogen bonding in solution: NMR spectroscopic approaches. *Coord. Chem. Rev.* **2020**, *407*, No. 213147.

(7) Wang, C.; Danovich, D.; Mo, Y.; Shaik, S. On The Nature of the Halogen Bond. *J. Chem. Theory Comput.* **2014**, *10*, 3726−3737.

(8) Wolters, L. P.; Schyman, P.; Pavan, M. J.; Jorgensen, W. L.; Bickelhaupt, F. M.; Kozuch, S. The many faces of halogen bonding: a review of theoretical models and methods. *Wiley Interdiscip. Rev.: Comput. Mol. Sci.* **2014**, *4*, 523−540.

(9) Cavallo, G.; Metrangolo, P.; Milani, R.; Pilati, T.; Priimagi, A.; Resnati, G.; Terraneo, G. The Halogen Bond. *Chem. Rev.* **2016**, *116*, 2478−2601.

(10) Kolář, M. H.; Hobza, P. Computer Modeling of Halogen Bonds and Other σ-Hole Interactions. *Chem. Rev.* **2016**, *116*, 5155−5187.

(11) Řezáč, J.; Hobza, P. Benchmark Calculations of Interaction Energies in Noncovalent Complexes and Their Applications. *Chem. Rev.* **2016**, *116*, 5038−5071.

(12) Oliveira, V.; Kraka, E.; Cremer, D. Quantitative Assessment of Halogen Bonding Utilizing Vibrational Spectroscopy. *Inorg. Chem.* **2017**, *56*, 488−502.

(13) Graton, J.; Rahali, S.; Le Questel, J.-Y.; Montavon, G.; Pilmé, J.; Galland, N. Spin−orbit coupling as a probe to decipher halogen bonding. *Phys. Chem. Chem. Phys.* **2018**, *20*, 29616−29624.

(14) Thirman, J.; Engelage, E.; Huber, S. M.; Head-Gordon, M. Characterizing the interplay of Pauli repulsion, electrostatics, dispersion and charge transfer in halogen bonding with energy decomposition analysis. *Phys. Chem. Chem. Phys.* **2018**, *20*, 905−915.

(15) Shaw, R. A.; Hill, J. G. A Simple Model for Halogen Bond Interaction Energies. *Inorganics* **2019**, *7*, 19.

(16) Alkorta, I.; Silva, A. F.; Popelier, P. L. A. An Interacting Quantum Atoms (IQA) and Relative Energy Gradient (REG) Study of the Halogen Bond with Explicit Analysis of Electron Correlation. *Molecules* **2020**, *25*, 2674.

(17) Inscoe, B.; Rathnayake, H.; Mo, Y. Role of Charge Transfer in Halogen Bonding. *J. Phys. Chem. A* **2021**, *125*, 2944−2953.

(18) Clark, T.; Hennemann, M.; Murray, J. S.; Politzer, P. Halogen bonding: the σ-hole. *J. Mol. Model.* **2007**, *13*, 291−296.

(19) Ciancaleoni, G.; Nunzi, F.; Belpassi, L. Charge Displacement Analysis—A Tool to Theoretically Characterize the Charge Transfer Contribution of Halogen Bonds. *Molecules* **2020**, *25*, 300.

(20) Ciancaleoni, G.; Belpassi, L. Disentanglement of orthogonal hydrogen and halogen bonds via natural orbital for chemical valence: A charge displacement analysis. *J. Comput. Chem.* **2020**, *41*, 1185−1193.

(21) Nunzi, F.; Cesario, D.; Tarantelli, F.; Belpassi, L. Halogen bond interaction: Role of hybridization and induction. *Chem. Phys. Lett.* **2021**, *771*, No. 138522.

(22) Laurence, C.; Queignec-Cabanetos, M.; Dziembowska, T.; Queignec, R.; Wojtkowiak, B. 1-Iodoacetylenes. 1. Spectroscopic evidence of their complexes with Lewis bases. A spectroscopic scale of soft basicity. *J. Am. Chem. Soc.* **1981**, *103*, 2567−2573.

(23) Laurence, C.; Queignec-Cabanetos, M.; Wojtkowiak, B. 1-Iodoacetylenes. Part 2. Formation constants of their complexes with Lewis bases. *J. Chem. Soc., Perkin Trans. 2* **1982**, *2*, 1605−1610.

(24) Laurence, C.; Queignec-Cabanetos, M.; Wojtkowiak, B. 1-Iodoacétylènes. IV. Relations structure−réactivité pour la complexation des 1-iodoacétylènes substitués avec des bases de Lewis. *Can. J. Chem.* **1983**, *61*, 135−138.

(25) Aakeröy, C. B.; Baldrighi, M.; Desper, J.; Metrangolo, P.; Resnati, G. Supramolecular Hierarchy among Halogen-Bond Donors. *Chem. - Eur. J.* **2013**, *19*, 16240−16247.

(26) Zhang, X.; Liu, G.; Ciborowski, S.; Wang, W.; Gong, C.; Yao, Y.; Bowen, K. Spectroscopic Measurement of a Halogen Bond Energy. *Angew. Chem., Int. Ed.* **2019**, *58*, 11400−11403.

(27) Rissanen, K. Halogen bonded supramolecular complexes and networks. *CrystEngComm* **2008**, *10*, 1107−1113.

(28) Dang, Q. M.; Simpson, J. H.; Parish, C. A.; Leopold, M. C. Evaluating Halogen-Bond Strength as a Function of Molecular Structure Using Nuclear Magnetic Resonance Spectroscopy and Computational Analysis. *J. Phys. Chem. A* **2021**, *125*, 9377−9393.

(29) Brammer, L.; Mínguez Espallargas, G.; Libri, S. Combining metals with halogen bonds. *CrystEngComm* **2008**, *10*, 1712−1727.

(30) Viger-Gravel, J.; Leclerc, S.; Korobkov, I.; Bryce, D. L. Direct Investigation of Halogen Bonds by Solid-State Multinuclear Magnetic Resonance Spectroscopy and Molecular Orbital Analysis. *J. Am. Chem. Soc.* **2014**, *136*, 6929−6942.

(31) Szell, P. M. J.; Grébert, L.; Bryce, D. L. Rapid Identification of Halogen Bonds in Co-Crystalline Powders via ^{127}I Nuclear Quadrupole Resonance Spectroscopy. *Angew. Chem., Int. Ed.* **2019**, *58*, 13479−13485.

(32) Xu, Y.; Szell, P. M. J.; Kumar, V.; Bryce, D. L. Solid-state NMR spectroscopy for the analysis of element-based non-covalent interactions. *Coord. Chem. Rev.* **2020**, *411*, No. 213237.

(33) Lu, J.; Scheiner, S. Effects of Halogen, Chalcogen, Pnicogen, and Tetrel Bonds on IR and NMR Spectra. *Molecules* **2019**, *24*, 2822.

(34) Libri, S.; Jasim, N. A.; Perutz, R. N.; Brammer, L. Metal Fluorides Form Strong Hydrogen Bonds and Halogen Bonds: Measuring Interaction Enthalpies and Entropies in Solution. *J. Am. Chem. Soc.* **2008**, *130*, 7842−7844.

(35) Beweries, T.; Brammer, L.; Jasim, N. A.; McGrady, J. E.; Perutz, R. N.; Whitwood, A. C. Energetics of Halogen Bonding of Group 10 Metal Fluoride Complexes. *J. Am. Chem. Soc.* **2011**, *133*, 14338−14348.

(36) Smith, D. A.; Beweries, T.; Blasius, C.; Jasim, N.; Nazir, R.; Nazir, S.; Robertson, C. C.; Whitwood, A. C.; Hunter, C. A.; Brammer, L.; Perutz, R. N. The Contrasting Character of Early and Late Transition Metal Fluorides as Hydrogen Bond Acceptors. *J. Am. Chem. Soc.* **2015**, *137*, 11820−11831.

(37) Pike, S. J.; Hunter, C. A.; Brammer, L.; Perutz, R. N. Benchmarking of Halogen Bond Strength in Solution with Nickel Fluorides: Bromine versus Iodine and Perfluoroaryl versus Perfluoroalkyl Donors. *Chem. - Eur. J.* **2019**, *25*, 9237−9241.

(38) Joksch, M.; Agarwala, H.; Ferro, M.; Michalik, D.; Spannenberg, A.; Beweries, T. A Comparative Study on the Thermodynamics of Halogen Bonding of Group 10 Pincer Fluoride Complexes. *Chem. - Eur. J.* **2020**, *26*, 3571−3577.

(39) Thangavadivale, V.; Aguiar, P. M.; Jasim, N. A.; Pike, S. J.; Smith, D. A.; Whitwood, A. C.; Brammer, L.; Perutz, R. N. Self-complementary nickel halides enable multifaceted comparisons of intermolecular halogen bonds: fluoride ligands vs. other halides. *Chem. Sci.* **2018**, *9*, 3767−3781.

(40) Chierotti, M. R.; Rossin, A.; Gobetto, R.; Peruzzini, M. Interaction between a Transition-Metal Fluoride and a Transition-Metal Hydride: Water-Mediated Hydrofluoric Acid Evolution Following Fluoride Solvation. *Inorg. Chem.* **2013**, *52*, 12616−12623.

(41) Leclerc, M. C.; Bayne, J. M.; Lee, G. M.; Gorelsky, S. I.; Vasiliu, M.; Korobkov, I.; Harrison, D. J.; Dixon, D. A.; Baker, R. T. Perfluoroalkyl Cobalt(III) Fluoride and Bis(perfluoroalkyl) Complexes: Catalytic Fluorination and Selective Difluorocarbene Formation. *J. Am. Chem. Soc.* **2015**, *137*, 16064−16073.

(42) Cronin, L.; Higgitt, C. L.; Karch, R.; Perutz, R. N. Rapid Intermolecular Carbon−Fluorine Bond Activation of Pentafluoropyridine at Nickel(0): Comparative Reactivity of Fluorinated Arene and Fluorinated Pyridine Derivatives. *Organometallics* **1997**, *16*, 4920−4928.

(43) Zilm, K. W.; Conlin, R. T.; Grant, D. M.; Michl, J. Low-temperature natural-abundance carbon-13 NMR spectroscopy of matrix-isolated species. The anisotropy of the shielding tensor in ethylene. *J. Am. Chem. Soc.* **1978**, *100*, 8038−8039.

(44) Kaupp, M. *Interpretation of NMR Chemical Shifts*, Kaupp, M.; Bühl, M.; Malkin, V. G., Eds.; Wiley-VCH: Weinheim, 2004; pp 293−306.

(45) Autschbach, J. Analyzing NMR shielding tensors calculated with two-component relativistic methods using spin-free localized molecular orbitals. *J. Chem. Phys.* **2008**, *128*, No. 164112.

(46) Autschbach, J.; Zheng, S. Analyzing Pt chemical shifts calculated from relativistic density functional theory using localized orbitals: The role of Pt 5d lone pairs. *Magn. Reson. Chem.* **2008**, *46*, S45−S55.

(47) Widdifield, C. M.; Schurko, R. W. Understanding chemical shielding tensors using group theory, MO analysis, and modern density-functional theory. *Concepts Magn. Reson., Part A* **2009**, *34*, 91−123.

(48) Viesser, R. V.; Ducati, L. C.; Tormena, C. F.; Autschbach, J. The unexpected roles of σ and π orbitals in electron donor and acceptor group effects on the ^{13}C NMR chemical shifts in substituted benzenes. *Chem. Sci.* **2017**, *8*, 6570−6576.

(49) Viesser, R.; Ducati, L. C.; Tormena, C. F.; Autschbach, J. The halogen effect on the ^{13}C NMR chemical shift in substituted benzenes. *Phys. Chem. Chem. Phys.* **2018**, *20*, 11247−11259.

(50) Gordon, C. P.; Raynaud, C.; Andersen, R. A.; Copéret, C.; Eisenstein, O. Carbon-13 NMR Chemical Shift: A Descriptor for Electronic Structure and Reactivity of Organometallic Compounds. *Acc. Chem. Res.* **2019**, *52*, 2278−2289.

(51) Raynaud, C.; Norbert-Agaisse, E.; James, B. R.; Eisenstein, O. ^{31}P Chemical Shifts in Ru(II) Phosphine Complexes. A Computational Study of the Influence of the Coordination Sphere. *Inorg. Chem.* **2020**, *59*, 17038−17048.

(52) Transue, W. J.; Dai, Y.; Riu, M.-L. Y.; Wu, G.; Cummins, C. C. ^{31}P NMR Chemical Shift Tensors: Windows into Ruthenium Phosphinidene Complex Electronic Structures. *Inorg. Chem.* **2021**, *60*, 9254−9258.

(53) Viesser, R. V.; Tormena, C. F. Inverse halogen dependence in anion ^{13}C NMR. *Phys. Chem. Chem. Phys.* **2021**, *23*, 3019−3030.

(54) Gordon, C. P.; Lätsch, L.; Copéret, C. Nuclear Magnetic Resonance: A Spectroscopic Probe to Understand the Electronic Structure and Reactivity of Molecules and Materials. *J. Phys. Chem. Lett.* **2021**, *12*, 2072−2085.

(55) Moss, W. N.; Goroff, N. S. Theoretical Analysis of the ^{13}C NMR of Iodoalkynes upon Complexation with Lewis Bases. *J. Org. Chem.* **2005**, *70*, 802−808.

(56) Cerreia Vioglio, P.; Catalano, L.; Vasylyeva, V.; Nervi, C.; Chierotti, M. R.; Resnati, G.; Gobetto, R.; Metrangolo, P. Natural

Abundance ^{15}N and ^{13}C Solid-State NMR Chemical Shifts: High Sensitivity Probes of the Halogen Bond Geometry. *Chem. - Eur. J.* **2016**, *22*, 16819−16828.

(57) Grimme, S.; Antony, J.; Ehrlich, S.; Krieg, H. A consistent and accurate ab initio parametrization of density functional dispersion correction (DFT-D) for the 94 elements H-Pu. *J. Chem. Phys.* **2010**, *132*, No. 154104.

(58) Vilela Oliveira, D.; Laun, J.; Peintinger, M. F.; Bredow, T. BSSE-correction scheme for consistent gaussian basis sets of double- and triple-zeta valence with polarization quality for solid-state calculations. *J. Comput. Chem.* **2019**, *40*, 2364−2376.

(59) Pickard, C. J.; Mauri, F. All-electron magnetic response with pseudopotentials: NMR chemical shifts. *Phys. Rev. B* **2001**, *63*, No. 245101.

(60) Marenich, A. V.; Cramer, C. J.; Truhlar, D. G. Universal Solvation Model Based on Solute Electron Density and on a Continuum Model of the Solvent Defined by the Bulk Dielectric Constant and Atomic Surface Tensions. *J. Phys. Chem. B* **2009**, *113*, 6378−6396.

(61) Chang, C.; Pélissier, M.; Durand, P. Regular Two-Component Pauli-Like Effective Hamiltonians in Dirac Theory. *Phys. Scr.* **1986**, *34*, 394−404.

(62) Lenthe, E. v.; Baerends, E. J.; Snijders, J. G. Relativistic regular two-component Hamiltonians. *J. Chem. Phys.* **1993**, *99*, 4597−4610.

(63) Schreckenbach, G.; Ziegler, T. Calculation of NMR Shielding Tensors Using Gauge-Including Atomic Orbitals and Modern Density Functional Theory. *J. Phys. Chem. A* **1995**, *99*, 606−611.

(64) Perdew, J. P.; Burke, K.; Ernzerhof, M. Generalized Gradient Approximation Made Simple. *Phys. Rev. Lett.* **1996**, *77*, 3865−3868.

(65) Perdew, J. P.; Burke, K.; Ernzerhof, M. Generalized Gradient Approximation Made Simple [Phys. Rev. Lett. 77, 3865 (1996)]. *Phys. Rev. Lett.* **1997**, *78*, 1396.

(66) Wolff, S. K.; Ziegler, T.; van Lenthe, E.; Baerends, E. J. Density functional calculations of nuclear magnetic shieldings using the zeroth-order regular approximation (ZORA) for relativistic effects: ZORA nuclear magnetic resonance. *J. Chem. Phys.* **1999**, *110*, 7689−7698.

(67) van Lenthe, E.; Baerends, E. J. Optimized Slater-type basis sets for the elements 1−118. *J. Comput. Chem.* **2003**, *24*, 1142−1156.

(68) Autschbach, J. The role of the exchange-correlation response kernel and scaling corrections in relativistic density functional nuclear magnetic shielding calculations with the zeroth-order regular approximation. *Mol. Phys.* **2013**, *111*, 2544−2554.

(69) Castro, A. C.; Fliegl, H.; Cascella, M.; Helgaker, T.; Repisky, M.; Komorovsky, S.; Medrano, M. Á.; Quiroga, A. G.; Swart, M. Four-component relativistic ^{31}P NMR calculations for trans-platinum(II) complexes: importance of the solvent and dynamics in spectral simulations. *Dalton Trans.* **2019**, *48*, 8076−8083.

(70) Castro, A. C.; Balcells, D.; Repisky, M.; Helgaker, T.; Cascella, M. First-Principles Calculation of ^{1}H NMR Chemical Shifts of Complex Metal Polyhydrides: The Essential Inclusion of Relativity and Dynamics. *Inorg. Chem.* **2020**, *59*, 17509−17518.

(71) Kaupp, M.; Schattenberg, C. J.; Müller, R.; Reimann, M. Unusually Large Effects of Charge-assisted C−H···F Hydrogen Bonds to Anionic Fluorine in Organic Solvents: Computational Study of ^{19}F NMR Shifts versus Thermochemistry. *ChemistryOpen* **2022**, *11*, No. e202200146.

(72) Halbert, S.; Copéret, C.; Raynaud, C.; Eisenstein, O. Elucidating the Link between NMR Chemical Shifts and Electronic Structure in d^0 Olefin Metathesis Catalysts. *J. Am. Chem. Soc.* **2016**, *138*, 2261−2272.

(73) Yamamoto, K.; Gordon, C. P.; Liao, W.-C.; Copéret, C.; Raynaud, C.; Eisenstein, O. Orbital Analysis of Carbon-13 Chemical Shift Tensors Reveals Patterns to Distinguish Fischer and Schrock Carbenes. *Angew. Chem., Int. Ed.* **2017**, *56*, 10127−10131.

(74) Gordon, C. P.; Yamamoto, K.; Liao, W.-C.; Allouche, F.; Andersen, R. A.; Copéret, C.; Raynaud, C.; Eisenstein, O. Metathesis Activity Encoded in the Metallacyclobutane Carbon-13 NMR Chemical Shift Tensors. *ACS Cent. Sci.* **2017**, *3*, 759−768.

(75) Gordon, C. P.; Shirase, S.; Yamamoto, K.; Andersen, R. A.; Eisenstein, O.; Copéret, C. NMR chemical shift analysis decodes olefin oligo- and polymerization activity of d^0 group 4 metal complexes. *Proc. Natl. Acad. Sci. U.S.A.* **2018**, *115*, E5867−E5876.

(76) Gordon, C. P.; Yamamoto, K.; Searles, K.; Shirase, S.; Andersen, R. A.; Eisenstein, O.; Copéret, C. Metal alkyls programmed to generate metal alkylidenes by α-H abstraction: prognosis from NMR chemical shift. *Chem. Sci.* **2018**, *9*, 1912−1918.

(77) Gordon, C. P.; Culver, D. B.; Conley, M. P.; Eisenstein, O.; Andersen, R. A.; Copéret, C. π-Bond Character in Metal−Alkyl Compounds for C−H Activation: How, When, and Why? *J. Am. Chem. Soc.* **2019**, *141*, 648−656.

(78) Gordon, C. P.; Copéret, C. Metal Alkyls with Alkylidynic Metal-Carbon Bond Character: Key Electronic Structures in Alkane Metathesis Precatalysts. *Angew. Chem., Int. Ed.* **2020**, *59*, 7035−7041.

(79) Wiberg, K. B.; Hammer, J. D.; Zilm, K. W.; Cheeseman, J. R.; Keith, T. A. NMR Chemical Shifts. 1. The Role of Relative Atomic Orbital Phase in Determining the Sign of the Paramagnetic Terms: ClF, CH$_3$F, CH$_3$NH$_3$$^+$, FNH$_3$$^+$, and HC⋮CF. *J. Phys. Chem. A* **1998**, *102*, 8766−8773.

(80) Alexakos, L. G.; Cornwell, C. D. NMR Spectra of ClF$_3$ and ClF: Gaseous Spectra and Gas-to-Liquid Shifts. *J. Chem. Phys.* **1964**, *41*, 2098−2107.

(81) Cornwell, C. D. Interpretation of the Chemical Shift of ClF. *J. Chem. Phys.* **1966**, *44*, 874−880.

(82) Wiberg, K. B.; Zilm, K. W. ^{19}F NMR Chemical Shifts. 1. Aliphatic Fluorides. *J. Org. Chem.* **2001**, *66*, 2809−2817.

(83) Häller, L. J. L.; Mas-Marzá, E.; Cybulski, M. K.; Sanguramath, R. A.; Macgregor, S. A.; Mahon, M. F.; Raynaud, C.; Russell, C. A.; Whittlesey, M. K. Computation provides chemical insight into the diverse hydride NMR chemical shifts of [Ru(NHC)$_4$(L)H]$^{0/+}$ species (NHC = N-heterocyclic carbene; L = vacant, H$_2$, N$_2$, CO, MeCN, O$_2$, P$_4$, SO$_2$, H$^−$, F$^−$ and Cl$^−$) and their [Ru(R$_2$PCH$_2$CH$_2$PR$_2$)$_2$(L)H]$^+$ congeners. *Dalton Trans.* **2017**, *46*, 2861−2873.

(84) Ruiz-Morales, Y.; Schreckenbach, G.; Ziegler, T. Origin of the Hydridic ^{1}H NMR Chemical Shift in Low-Valent Transition-Metal Hydrides. *Organometallics* **1996**, *15*, 3920−3923.

(85) Khaliullin, R. Z.; Cobar, E. A.; Lochan, R. C.; Bell, A. T.; Head-Gordon, M. Unravelling the Origin of Intermolecular Interactions Using Absolutely Localized Molecular Orbitals. *J. Phys. Chem. A* **2007**, *111*, 8753−8765.

(86) Khaliullin, R. Z.; Bell, A. T.; Head-Gordon, M. Analysis of charge transfer effects in molecular complexes based on absolutely localized molecular orbitals. *J. Chem. Phys.* **2008**, *128*, No. 184112.

(87) Khaliullin, R. Z.; Head-Gordon, M.; Bell, A. T. An efficient self-consistent field method for large systems of weakly interacting components. *J. Chem. Phys.* **2006**, *124*, No. 204105.

(88) Horn, P. R.; Sundstrom, E. J.; Baker, T. A.; Head-Gordon, M. Unrestricted absolutely localized molecular orbitals for energy decomposition analysis: Theory and applications to intermolecular interactions involving radicals. *J. Chem. Phys.* **2013**, *138*, No. 134119.

(89) Thangavadivale, V. G.; Tendera, L.; Bertermann, R.; Radius, U.; Beweries, T.; Perutz, R. N. Solution and solid-state studies of hydrogen and halogen bonding with N-heterocyclic carbene supported nickel(II) fluoride complexes. *Faraday Discuss.* **2023**, No. 00171C.

(90) Dovesi, R.; Saunders, V. R.; Roetti, C.; Orlando, R.; Zicovich-Wilson, C. M.; Pascale, F.; Civalleri, B.; Doll, K.; Harrison, N. M.; Bush, I. J.; D'Arco, P.; Llunell, M.; Causà, M.; Noël, Y.; Maschio, L.; Erba, A.; Rerat, M.; Casassa, S. *CRYSTAL17 Program*; University of Torino: Torino, 2017.

(91) Dovesi, R.; Erba, A.; Orlando, R.; Zicovich-Wilson, C. M.; Civalleri, B.; Maschio, L.; Rérat, M.; Casassa, S.; Baima, J.; Salustro, S.; Kirtman, B. Quantum-mechanical condensed matter simulations with CRYSTAL. *Wiley Interdiscip. Rev.: Comput. Mol. Sci.* **2018**, *8*, No. e1360.

(92) Adamo, C.; Barone, V. Toward reliable density functional methods without adjustable parameters: The PBE0 model. *J. Chem. Phys.* **1999**, *110*, 6158−6170.

(93) Heyd, J.; Scuseria, G. E.; Ernzerhof, M. Hybrid functionals based on a screened Coulomb potential. *J. Chem. Phys.* **2003**, *118*, 8207−8215.

(94) Frisch, M. J.; et al. *Gaussian 09*; Gaussian Inc.: Wallingford, CT, 2016.

(95) Jensen, F. Segmented Contracted Basis Sets Optimized for Nuclear Magnetic Shielding. *J. Chem. Theory Comput.* **2015**, *11*, 132−138.

(96) Jensen, F. Unifying General and Segmented Contracted Basis Sets. Segmented Polarization Consistent Basis Sets. *J. Chem. Theory Comput.* **2014**, *10*, 1074−1085.

(97) Giannozzi, P.; Baroni, S.; Bonini, N.; et al. QUANTUM ESPRESSO: a modular and open-source software project for quantum simulations of materials. *J. Phys.: Condens. Matter* **2009**, *21*, No. 395502.

(98) te Velde, G.; Bickelhaupt, F. M.; Baerends, E. J.; Fonseca Guerra, C.; van Gisbergen, S. J. A.; Snijders, J. G.; Ziegler, T. Chemistry with ADF. *J. Comput. Chem.* **2001**, *22*, 931−967.

(99) Baerends, E. J. et al. ADF Program. In *SCM, Theoretical Chemistry*; Vrije Universiteit: Amsterdam, The Netherlands, 2019.

(100) Ditchfield, R. Self-consistent perturbation theory of diamagnetism. *Mol. Phys.* **1974**, *27*, 789−807.

(101) Komorovský, S.; Repiský, M.; Malkina, O. L.; Malkin, V. G.; Malkin Ondík, I.; Kaupp, M. A fully relativistic method for calculation of nuclear magnetic shielding tensors with a restricted magnetically balanced basis in the framework of the matrix Dirac−Kohn−Sham equation. *J. Chem. Phys.* **2008**, *128*, No. 104101.

(102) Komorovský, S.; Repiský, M.; Malkina, O. L.; Malkin, V. G. Fully relativistic calculations of NMR shielding tensors using restricted magnetically balanced basis and gauge including atomic orbitals. *J. Chem. Phys.* **2010**, *132*, No. 154101.

(103) Repisky, M.; Komorovsky, S.; Kadek, M.; Konecny, L.; Ekström, U.; Malkin, E.; Kaupp, M.; Ruud, K.; Malkina, O. L.; Malkin, V. G. ReSpect: Relativistic spectroscopy DFT program package. *J. Chem. Phys.* **2020**, *152*, No. 184101.

(104) Jensen, F. Polarization consistent basis sets: Principles. *J. Chem. Phys.* **2001**, *115*, 9113−9125.

(105) Jensen, F. Polarization consistent basis sets. II. Estimating the Kohn−Sham basis set limit. *J. Chem. Phys.* **2002**, *116*, 7372−7379.

(106) Glendening, E. D.; Landis, C. R.; Weinhold, F. NBO 6.0: Natural bond orbital analysis program. *J. Comput. Chem.* **2013**, *34*, 1429−1437.

(107) Glendening, E. D.; Badenhoop, J. K.; Reed, A. E.; Carpenter, J. E.; Bohmann, J. A.; Morales, C. M.; Landis, C. R.; Weinhold, F. *NBO 6.0*; Theoretical Chemistry Institute, University of Wisconsin: Madison, 2013. www.chem.wisc.edu/~nbo6.

(108) Shao, Y.; Gan, Z.; Epifanovsky, E.; et al. Advances in molecular quantum chemistry contained in the Q-Chem 4 program package. *Mol. Phys.* **2015**, *113*, 184−215.

(109) Álvarez-Moreno, M.; de Graaf, C.; López, N.; Maseras, F.; Poblet, J.; Bo, C. Managing the computational chemistry big data problem: the ioChem-BD platform. *J. Chem. Inf. Model.* **2015**, *55*, 95−103.

📖 Recommended by ACS

Unusual Actinyl Complexes with a Redox-Active N,S-Donor Ligand

Jing Su, Ping Yang, *et al.*
JUNE 30, 2023
INORGANIC CHEMISTRY　　　　　　　READ 🗗

Inelastic Neutron Scattering Measurement of the Ground State Tunneling Gap in Tb and Ho Analogues of a Dy Field-Induced Single-Molecule Magnet

Aiden M. Atkin, Colette Boskovic, *et al.*
JANUARY 11, 2023
INORGANIC CHEMISTRY　　　　　　　READ 🗗

Experimentally Established ¹⁵N NMR Absolute Shielding Scale for Theoretical Calculations

Ilya G. Shenderovich.
JUNE 21, 2023
THE JOURNAL OF PHYSICAL CHEMISTRY A　　　　READ 🗗

Reduction of Nitrous Oxide and Binding of Carbon Dioxide by Acenaphthene-1,2-diimine Aluminum Compounds

Tatyana S. Koptseva, Igor L. Fedushkin, *et al.*
MAY 02, 2023
ORGANOMETALLICS　　　　　　　READ 🗗

Get More Suggestions >